High-Performance Silver Window Electrodes for Top-Illuminated Organic Photovoltaics Using an Organo-molybdenum Oxide Bronze Interlayer

Martin S. Tyler,[†] Marc Walker,[‡] and Ross A. Hatton*,[†]

[†]Department of Chemistry, University of Warwick, Coventry CV4 7AL, U.K.
[‡]Department of Physics, University of Warwick, Coventry CV4 7AL, U.K.

S *Supporting Information*

ABSTRACT: We report an organo-molybdenumn oxide bronze that enables the fabrication of high-performance silver window electrodes for top-illuminated solution processed organic photovoltaics without complicating the process of device fabrication. This hybrid material combines the function of wide-band-gap interlayer for efficient hole extraction with the role of metal electrode seed layer, enabling the fabrication of highly transparent, low-sheet-resistance silver window electrodes. Additionally it is also processed from ethanol, which ensures orthogonality with a large range of solution processed organic semiconductors. The key organic component is the low cost small molecule 3-mercaptopropionic acid, which (i) promotes metal film formation and imparts robustness at low metal thickness, (ii) reduces the contact resistance at the Ag/molybdenumn oxide bronze interface, (iii) and greatly improves the film forming properties. Silver electrodes with a thickness of 8 nm deposited by simple vacuum evaporation onto this hybrid interlayer have a sheet resistance as low as 9.7 Ohms per square and mean transparency ∼80% over the wavelength range 400−900 nm without the aid of an antireflecting layer, which makes them well-matched to the needs of organic photovoltaics and applicable to perovskite photovoltaics. The application of this hybrid material is demonstrated in two types of top-illuminated organic photovoltaic devices.

KEYWORDS: electrode, photovoltaic, top-illuminated, molybdenum oxide, charge transport layer
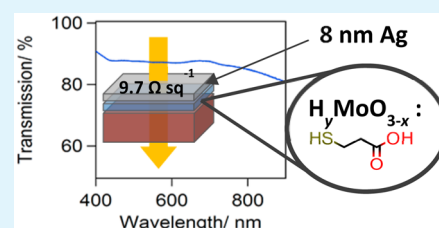
INTRODUCTION

It is widely recognized that the full-cost advantage of solution processed organic and perovskite photovoltaics (OPV and PPV) over conventional crystalline silicon PV will only be achieved if an alternative to the conducting oxide coated glass electrodes used in the current generations of OPV and PPV is forthcoming. This is primarily because conducting oxides are poorly compatible with low cost roll-to-roll manufacturing processes.[1] One promising approach to address this challenge is to fabricate devices with a top-illuminated architecture, using an optically thin metal film as the transparent top electrode,[2,3] which removes the need for conducting oxide coated glass and increases the range of potential applications by giving more flexibility in terms of the materials used as the supporting substrate. For example, for integrating PVs into buildings and vehicles it is desirable to fabricate onto flexible steel or Al substrates rather than glass.[4] Vacuum evaporation is well-established in the packaging industry as a low cost, large area deposition method for the fabrication of thin metal films and is compatible with roll-to-roll deposition onto flexible substrates, as well as offering the necessary high degree of control over metal film thickness.[5] The potential of this approach to achieve comparable device performance to conventional device architectures based on a conducting oxide window electrode has been demonstrated in wholly vacuum deposited small molecule OPVs by the group of Leo,[6] using Ag as the base

metal for the transparent electrode. Ag is the metal of choice for this application because it has the highest conductivity[7] and the lowest optical absorbance[8] of the earth abundant metals over the visible spectrum, combined with relatively high stability toward oxidation in air. However, Ag also has a high surface energy and so thin films of this metal have a high percolation thickness of >10 nm, below which they form a discontinuous island like structure which is poorly conductive, and strongly absorbs visible light due to excitation of localized surface plasmons.[9] This limitation is particularly pronounced when evaporating Ag onto polymer and small molecule semiconductors because Ag tends to bind weakly to these classes of materials and the high surface energy of Ag is a powerful driver for the formation of Ag nanoparticles.[6,10]

In practice, for PV applications the sheet resistance of the window electrode cannot realistically exceed 10 Ω sq^{-1} without incurring an unacceptable loss in device fill-factor or requiring a relatively dense array of opaque current carrying bus-bars.[11,12] Additionally, the electrode transparency across the wavelength range λ= 400−900 nm must be ≥80% to be competitive with a 10 Ω sq^{-1} conducting oxide coated glass (e.g., F:SnO$_2$ and Sn:In$_2$O$_3$).[11] In recent years Schubert et al.[6] and Yang et al.[13]

have shown that it is possible to achieve a sheet resistance of $\sim$19 and $\sim$16 Ω sq^{-1} respectively for sub-10 nm Ag window electrodes in top-illuminated OPV and PPVs, with peak transparencies of $\sim$80%, although with much lower transparency in other useful parts of the spectrum. In both cases the Ag electrodes were fabricated by depositing a 1 nm Au seed layer immediately prior to Ag deposition. The disadvantages of that approach are (i) the cost incurred by adding an extra step to the fabrication process.; (ii) and the use of Au which is almost certainly too costly to be used in PV applications, even at such a low thickness.[14] It is also unclear as to the extent to which the stability of the Ag window electrode is affected when using a 1 nm Au seed layer. Co-depositing Ag with Ca in conjunction with a 1 nm Al seed layer has also been shown to be a promising approach to enable the fabrication of Ag-based window electrodes for top-illuminated OPV, offering a transparency greater than 90% over a large portion of the visible spectrum. However, the sheet resistance of these Al:Ca:Ag electrodes; 27.3 Ω sq^{-1}, is arguably too high to be implemented in PVs, and the susceptibility of Ca to oxidation is a major drawback.[15] What is needed is a means of enabling the formation of highly conductive, sub-10 nm Ag films on the top surface of OPV and PPVs that does not complicate the process of device fabrication and is applicable to solution processed device architectures, since it is widely regarded that solution processing offers the lowest cost path to PV device fabrication.[16,17]

Herein, we report the development of an organomolybdenumn oxide bronze, MPA:H_yMoO_{3-x}, where MPA is 3-mercaptopropionic acid, that combines the function of wide band gap interlayer for the efficient extraction of holes from organic semiconductors, with the role of seed layer for the formation of robust sub-10 nm Ag films for top-illuminated solution processed PV devices. Transition metal charge extraction layers, including transition metal bronzes,[18,19] are an essential component of high performance OPVs[3,20,21] and so, unlike the use of an ultrathin Au interlayer, the hybrid reported herein does not complicate the process of device fabrication. Additionally, the composite is processed from ethanol which is environmentally sustainable and ensures orthogonality with a large range of solution processed organic semiconductors.

■ RESULTS AND DISCUSSION

MoO_{3-x} is one of the most widely used hole-extraction materials in organic electronics and is typically deposited by vacuum evaporation, although solution processing methods, which invariably include a postdeposition annealing step, have also begun to emerge.[17,21−24] Depositing very thin films (i.e., 5−10 nm) of metal oxides from solution directly onto organic semiconductors is particularly challenging due to the need for solvent orthogonality between layers and the constraint on postdeposition annealing temperature imposed by the underlying organic semiconductor. One transition metal oxide that has been successfully applied from solution directly onto the surface of organic semiconductors is molybdenum oxide bronze; H_yMoO_{3-x}.[18,25,26] Herein the method used for H_yMoO_{3-x} synthesis is an adaptation of this approach, modified to include additional heating steps and an increased reaction time, as detailed in the Experimental Section. In this wide band gap semiconductor oxygen vacancies and hydrogen serve as deep and shallow n-type dopants, respectively.[24] MPA was added to alcoholic solutions of H_yMoO_{3-x} and all films were

briefly annealed at 80 °C under nitrogen to remove residual solvent. Because of the very mild annealing temperature thin films of this material are essentially amorphous as shown by the absence of well-defined peaks in the X-ray diffraction pattern (Figure S1).

X-ray photoelectron spectroscopy (XPS) was used to determine how incorporation of MPA into H_yMoO_{3-x} alters its electronic structure. All spectroscopic characterization was performed for samples with loadings of 0.29 or 0.86 MPA molecules per Mo atom, which was found to be the optimal loading for OPV applications, as detailed in subsequent sections of this paper. It is evident from the high resolution XPS (HRXPS) spectrum of the Mo 3d region of H_yMoO_{3-x} without MPA; (Figure 1a) that Mo is present in both the 6+ and 5+

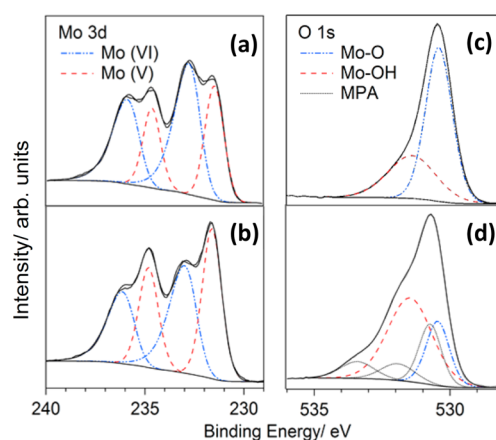**Figure 1.** HRXPS binding energy spectra of (a) the Mo 3d regions in H_yMoO_{3-x} and (b) MPA doped H_yMoO_{3-x}(c) the O 1s regions for H_yMoO_{3-x} (d),and MPA doped H_yMoO_{3-x}. The MPA:Mo ratio in MPA doped samples is 0.86:1. The O 1s peak assignments associated with MPA in panel d are C═O (531.9 eV) C−OH (533.4 eV) and COO⁻ (530.7 eV).

oxidation states. The ratio of the Mo 3d$_{5/2}$ peaks at $\sim$232.6 and $\sim$231.4 eV, which are assigned to Mo^{6+} and Mo^{5+} respectively, is 1:0.6, which yields a mean Mo oxidation state of 5.62. The O 1s region of the spectrum (Figure 1c) can be fitted with two components at $\sim$530.4 and $\sim$531.4 eV which are assigned to Mo−OH and Mo−O−Mo (or Mo═O) chemical environments, respectively.[22,23,27] If it is assumed that hydrogenation is the only source of reduction, then the average Mo oxidation state calculated from the O 1s peak intensities is 5.67. The difference between this value and the actual value of 5.62, determined from the Mo^{6+}:Mo^{5+} peak intensities, can be assigned to the presence of oxygen vacancy defects and so the average stoichiometry of the bronze is estimated to be $H_{0.24}MoO_{2.95}$.

It is evidence from Figure 1b that addition of MPA results in a further reduction in the average Mo oxidation state because the Mo^{6+}:Mo^{5+} ratio is reduced to 5.51 for an MPA:Mo loading of 0.86:1. The O 1s region for H_yMoO_{3-x} with MPA (Figure 1d) includes three additional peaks corresponding to two oxygen environments in carboxylic acid; C═O (531.9 eV) and C−OH (533.4 eV),[28] and one in deprotonated carboxylic acid; COO⁻ (530.7 eV).[29] By constraining the Mo−O and Mo−OH peak positions and widths to those in Figure 1c and assuming a MPA:H_yMoO_3 ratio of 0.86:1 (confirmed from the XPS survey scan), the deconvolution of the O 1s peak is as given in Figure 1d. It is evident from Figure 1(d) that the peak attributed to

Mo−OH at 531.5 eV has increased in intensity with respect to the Mo−O peak at 530.5 eV, which is further evidence for the reduction of $H_yMoO_{3−x}$ by MPA. It is also evident that there is a significant amount of deprotonated MPA in the $H_yMoO_{3−x}$ film and so the additional Mo reduction upon doping with MPA can be attributed to donation of hydrogen by the carboxylic acid group resulting in the formation of Mo−OH. The HRXPS spectrum of the S 2p region (Figure S2) is consistent with this conclusion, since the sulfur is primarily present as unreacted thiol.

The ultraviolet photoelectron spectroscopy (UPS) spectra shown in Figure 2 corroborates the conclusion that MPA serves
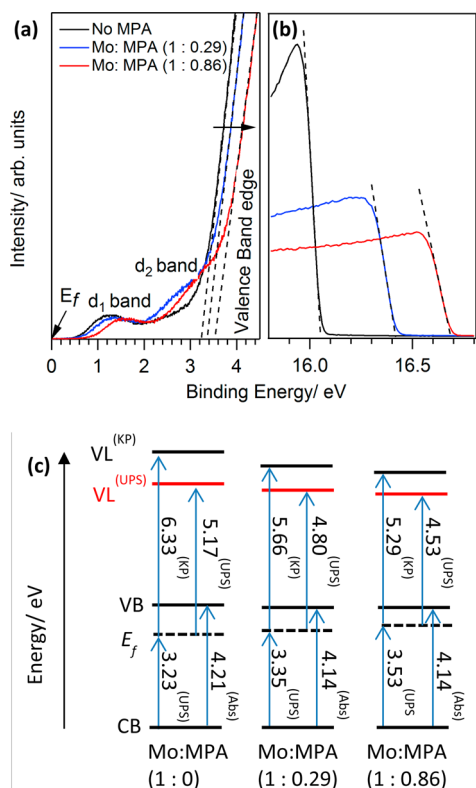

Figure 2. UPS spectra of the valence band edge (a) and secondary-electron cutoff (b) of MPA:$H_yMoO_{3−x}$ films with increasing MPA loading.; (c) Energy levels of $H_yMoO_{3−x}$ films with respect to the vacuum level (VL) for loadings of 1:0, 1:0.29, and 1:0.86 Mo:MPA derived from UPS, KP, and absorption spectra Tauc plots.

as a source of hydrogen, and therefore as a shallow *n*-type dopant, since the energy difference between the Fermi level (E_f) and the valence band (VB) edge increases from ∼3.21 eV with no MPA, to ∼3.35 and ∼3.61 eV with increasing MPA loading. The two small peaks in the bandgap, labeled d_1 and d_2, can be assigned to occupied defect states due to hydrogen insertion and oxygen vacancies, since both are known to be present in reduced molybdenum oxides.[24,30] The optical band gap of $H_yMoO_{3−x}$ was estimated to be ∼4.21 eV from the absorption spectrum by plotting $(\alpha h\nu)^2$ versus $h\nu$ in a Tauc plot (Figure S3). Upon addition of MPA the band gap was found to undergo a slight reduction to a value of ∼4.14 eV. The absorption coefficient of $H_yMoO_{3−x}$ films is increased from ∼0.2 to ∼0.3 $m^{−1}$ in the wavelength range λ = 400−600 nm and reduced by a commensurate amount for λ = 600−900 nm and so the mean value across the range λ = 400−900 nm is not significantly changed.

Addition of MPA to $H_yMoO_{3−x}$ also resulted in a reduction in its work function, as determined from the secondary-electron cutoff of the UPS spectra (Figure 2b) and measured using the Kelvin probe technique (KP). Figure 2c shows a schematic energy level diagram summarizing these data, along with the band gap estimated from absorption spectra Tauc plots (Figure S3). While UPS and KP show the same trend in work function the measurements made using UPS are consistently lower than that measured using the KP. This difference can in part be explained by the fact that UPS is known to measure the lowest work function, while the KP technique measures the average work function under the probe.[31,32] However, for UPS measurements the samples were also briefly exposed to the laboratory environment when loading into the UPS vacuum chamber, and so modification of the surface potential contribution to work function by surface contamination is likely. Conversely the KP measurements were made using a KP located in the same nitrogen filled glovebox as used for film deposition, and so measurements made using the KP technique are considered to be more reliable in this instance, a conclusion corroborated by the device studies described in a subsequent part of this paper. The work function measured using the KP is reduced from 6.33 eV (±0.14) for the $H_yMoO_{3−x}$ without MPA, to 5.66 eV (±0.06) and 5.29 eV (±0.15) after doping with MPA:Mo loadings of 0.29:1 and 0.86:1, respectively. Since the largest change in work function, $\Delta \approx 1.04$ eV, is much greater than the change in the position of E_f in the bandgap (Figure 2c), the MPA must be acting to lower the surface potential contribution to the work function in addition to changing the chemical potential. A similar decrease in the work function of $H_yMoO_{3−x}$ upon *n*-type doping with Cs has been reported by Li et al.[25,26] and in that case the change in work function was sufficiently large to enable its use as an electron extracting interfacial layer. For transition metal oxide hole-extraction layers efficient hole extraction from an organic semiconductor is only achieved when the oxide work function is higher or comparable to the ionization potential of the adjacent organic semiconductor.[33] In this case, even for the highest MPA doping level tested, the work function of $H_yMoO_{3−x}$:MPA should still be sufficiently large to ensure optimized interfacial energy level alignment with the HOMO of most donor-type organic semiconductors.[34] This conclusion is supported by the OPV device studies reported in a subsequent section of this paper.

Current−voltage analysis of unipolar diodes with the structure Au|$H_yMoO_{3−x}$|Ag (and Au) was used to determine the effect of MPA doping on the electrical conductivity of the bronze and its contact resistance with the Ag electrode (Figure S4a and b). For the Au | $H_yMoO_{3−x}$ | Ag diode conductivities of $3.94 \times 10^{−3}$ (±0.53 × $10^{−3}$), $3.80 \times 10^{−3}$ (±0.53 × $10^{−3}$), and $4.33 \times 10^{−3}$ S $m^{−1}$ (±0.68 × $10^{−3}$) were measured for films with a Mo:MPA loading of 1:0, 1:0.29 and 1:0.86 respectively. The small increase in the mean conductivity upon MPA doping is consistent with *n*-type doping and/or a reduction in contact resistance with the Ag electrode. Conversely, for the Au|$H_yMoO_{3−x}$|Au diodes conductivities of $1.50 \times 10^{−3}$ (±0.27 × $10^{−3}$)−$1.41 \times 10^{−3}$ (±0.35 × $10^{−3}$) and $1.14 \times 10^{−3}$ S $m^{−1}$ (±0.13 × $10^{−3}$) were measured for films with a Mo:MPA loading of 1:0, 1:0.29, and 1:0.86, respectively, and so the mean conductivity is slightly decreased with MPA loading, although again the change in conductivity with MPA loading is barely statistically significant even for the highest MPA loading. Taken together, these data show that there is a small reduction in

conductivity of the bronze when MPA is added, which is more than offset by the reduction in contact resistance when Ag is used as the electrode.

To investigate the film forming properties when deposited directly onto organic semiconductors two widely used bulk-heterojunctions (BHJs) were used as model substrates; namely, PTB7:PC$_{70}$BM and PCDTBT:PC$_{70}$BM (full chemical names given in Experimental Section). The morphology of a ~10 nm H$_y$MoO$_{3-x}$ film spin-cast directly onto a PTB7:PC$_{70}$BM BHJ film, measured using atomic force microscopy (AFM), is shown in Figure S5, from which it is evident that addition of MPA dramatically reduces the film roughness: The root-mean-square roughness was reduced from 4.3 ($\pm$0.5) to 2.0 nm ($\pm$0.3). Conversely, H$_y$MoO$_{3-x}$ films spun directly onto glass with and without MPA doping exhibit no significant difference in surface roughness (Figure S6) and so the difference in film roughness when deposited directly onto BHJ films can be attributed to improved wetting due to the presence of MPA, rather than suppression of aggregate formation in the H$_y$MoO$_{3-x}$ solution when MPA is added. This marked improvement in film forming properties is evidence that the H$_y$MoO$_{3-x}$ solution wets the organic semiconductor surface more readily when MPA is added, further evidence for which is provided by measurement of the static contact angle (Figure S7) of droplets of H$_y$MoO$_{3-x}$ solution on PTB7:PC$_{70}$BM BHJ films; < 2° with 1:0.86 MPA doping vs 19.53° ($\pm$3.6) without. H$_y$MoO$_{3-x}$ films spin-cast onto PCDTBT:PC$_{70}$BM showed no significant difference in surface roughness, although static contact angle measurements provided evidence of improved wetting; 13.1° ($\pm$2.5) with 1:0.29 MPA doping and 18.6° ($\pm$1.8) without (Figure S7).

To fabricate Ag window electrodes with properties comparable to that in top-illuminated OPV devices Ag films of thickness 8 nm were thermally evaporated onto H$_y$MoO$_{3-x}$ coated BHJ films supported on glass. Again the widely used BHJs PTB7:PC$_{70}$BM and PCDTBT:PC$_{70}$BM were used as model substrates. A Ag thickness of 8 nm was chosen because it was found to be the minimum needed to achieve the target sheet resistance (R_{sheet}) of ~10 Ω sq^{-1}, as measured using the Van der Paw method.[35] The results from a representative batch of electrodes on PTB7:PC$_{70}$BM films are shown in Figure 3a, which show that the mean R_{sheet} is decreased from 14.8 ($\pm$2.2) to 11.1 Ω sq^{-1} ($\pm$0.6) when MPA is added to H$_y$MoO$_{3-x}$ (MPA:Mo ratio of 0.86:1). The decrease in R_{sheet} correlates with a significant decrease in Ag film roughness, which is ~20% lower upon addition of MPA (Figure 4), primarily due to a smoother underlying Mo bronze layer (Figure S5). This reduction in electrode roughness inevitably decreases ohmic losses due to scattering of electrons, which offers a plausible explanation for the improvement in R_{sheet} upon addition of MPA. In addition to the ~25% reduction in sheet resistance the addition of MPA to the Mo bronze also greatly improves the electrode stability: After 70 h storage in nitrogen (<1 ppm of O$_2$ and H$_2$O) the R_{sheet} of films supported on MPA doped H$_y$MoO$_{3-x}$ was essentially unchanged at 11.5 Ω sq^{-1} ($\pm$0.7) (Figure 3a). In contrast R_{sheet} of Ag electrodes supported on H$_y$MoO$_{3-x}$ without MPA was either in the range 18.3 Ω sq^{-1} ($\pm$1.8) or was too high to measure ($R_{sheet} \geq$ 200000 Ω sq^{-1}). The AFM images in Figure 4 (and Figure S8) show that the surface roughness of Ag films supported on H$_y$MoO$_{3-x}$ without MPA greatly increases upon storage in nitrogen due to the formation of large aggregates which do not form when MPA is incorporated into the H$_y$MoO$_{3-x}$ underlayer. This data supports the conclusion that the MPA serves as a molecular
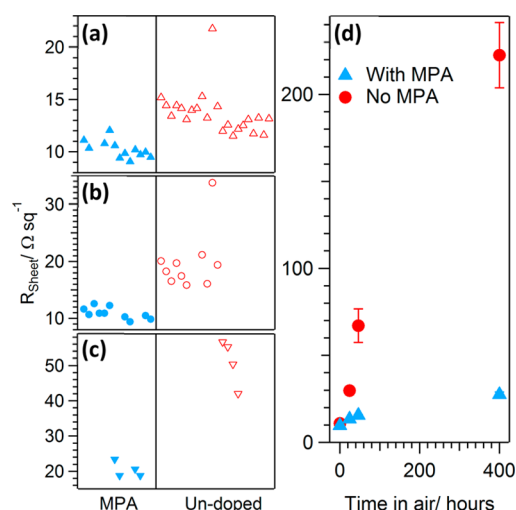

Figure 3. R_{sheet} of 8 nm Ag films supported on glass|PTB7:PC$_{70}$BM|H$_y$MoO$_{3-x}$ with 1:0.86 Mo:MPA in the H$_y$MoO$_{3-x}$ layer (filled shapes) and without MPA (empty shapes): (a) immediately after fabrication, (b) after 70 h in N$_2$, (c) after 70 h in air. (d) R_{sheet} of 8 nm Ag films supported on glass|PCDTBT:PC$_{70}$BM|H$_y$MoO$_{3-x}$ with and without 1:0.29 Mo:MPA doping as a function of time stored in air. In all cases, the electrode size was 1.8 × 1.8 cm.
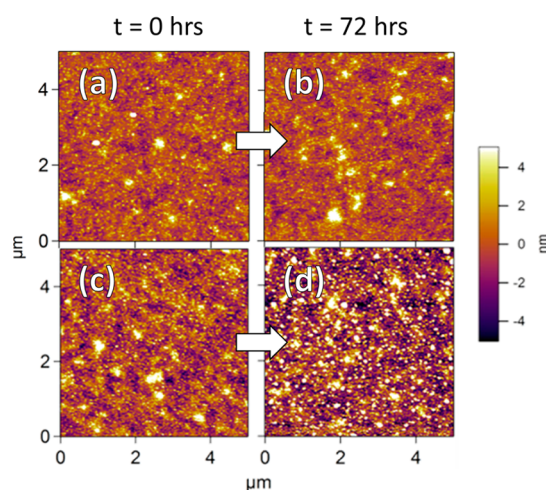

Figure 4. Morphology of 8 nm Ag film supported on glass|PTB7:PC$_{70}$BM|H$_y$MoO$_{3-x}$ with (a and b) and without (c and d) MPA doping at a MPA:Mo ratio of 0.86:1 immediately after fabrication (a and c) and after 72 h storage in N$_2$ (<1 ppm of O$_2$ and H$_2$O) (b and d).

adhesive, helping to bind Ag atoms onto the H$_y$MoO$_{3-x}$, and so counteract the thermodynamic instability in thin Ag films that stems from the high surface energy of this metal.

The stability of these films was further tested as a function of storage time in ambient air (20 °C and relative humidity 30−40%) (Figure 3a). After 70 h in air the sheet resistance of Ag films supported on MPA doped H$_y$MoO$_{3-x}$ had increased from 10.2 ($\pm$0.8) to 20.4 Ω sq^{-1} ($\pm$1.9). Without MPA the change was much more pronounced, since the R_{sheet} increased from 13.7 ($\pm$2.1) to 51.1 Ω sq^{-1} ($\pm$5.8). In both cases, the increase in R_{sheet} did not correlate with an increase in surface roughness, presumably due to the formation of a constraining silver oxide capping layer.

To test the generality of these results the same experiment was performed using PCDTBT:PC$_{70}$BM in place of

P7BT:PC$_{70}$BM. Again, the sheet resistance of the electrode is reduced when MPA is incorporated into the H$_y$MoO$_{3-x}$ layer, from 10.9 Ω sq^{-1} ($\pm$0.4) without MPA to 9.7 Ω sq^{-1} ($\pm$0.5) (MPA: Mo loading of 0.29:1), and for the latter there is no significant increase in the R_{sheet} when stored under N$_2$, even after 384 h. However, in this case the electrode without MPA in the H$_y$MoO$_{3-x}$ layer also exhibits good stability when stored under N$_2$. This result is attributed to the lower surface roughness of the underlying BHJ film; ~1.6 nm PCDTBT:PC$_{70}$BM vs ~2.8 nm for PTB7:PC$_{70}$BM, which results in a smoother H$_y$MoO$_{3-x}$ layer, which in turn results in a smoother more compact Ag electrode with higher intrinsic stability due to a reduced surface area (Figure S9). Conversely, as shown in Figure 3b, the difference in the rate of electrode degradation in ambient air is very pronounced. After 400 h the R_{sheet} of electrodes without MPA in the H$_y$MoO$_{3-x}$ layer increases by a factor of 20 times from 10.9 ($\pm$0.4) to 222.6 Ω sq^{-1} ($\pm$18.8), whereas those with MPA increased by less than a factor of 3 from 9.7 Ω sq^{-1} ($\pm$0.5) to 27.6 Ω sq^{-1} ($\pm$1.5).

The lower R_{sheet}, reduced contact resistance and improved stability of the electrodes on both model BHJs upon incorporation of MPA into the H$_y$MoO$_{3-x}$ layer is consistent with improved adhesion at the bronze-Ag interface. XPS studies were conducted to probe the nature of this interaction by acquiring spectra before and after depositing an ultrathin Ag film; 1.1 nm. To ensure no uncontrolled oxidation or contamination by air exposure the experiment was conducted under high vacuum with a Ag evaporation source colocated in the XPS chamber. It is evident from Figure 5 that the sulfur on
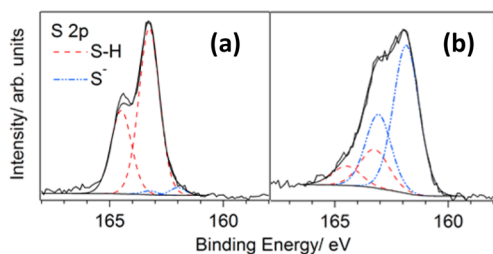

Figure 5. HRXPS spectra of H$_y$MoO$_{3-x}$:MPA S 2p region before (a) and after (b) deposition of 1.1 nm Ag.

the MPA molecules exists primarily in one chemical environment when incorporated into H$_y$MoO$_{3-x}$, which can be attributed to the free thiol,[36] with a very small proportion (1:29) existing as thiolate, possibly due to coordination with a Mo atom. Upon evaporation of a thin Ag layer the signal intensity reduced because the photoelectrons must now come from beneath the Ag overlayer. The ~1.4 eV reduction in the binding energy of the S 2p electrons upon Ag deposition is compelling evidence for thiolate-Ag bond formation.[36] The improvement in stability of the film under N$_2$ is therefore attributed to the binding interaction between the thiol functionality on MPA and the evaporated metal, which serves to help immobilize the incident Ag atoms when they arrive on the bronze surface, enabling the formation of dense conformal Ag films at low thickness.

Figure 6 shows the far-field transparency of 8 nm Ag electrodes on both PTB7:PC$_{70}$BM and PCDTBT:PC$_{70}$BM films over the wavelength range λ = 400−900 nm. On PTB7:PC$_{70}$BM, which has the higher surface roughness of the two BHJs, the mean transparency of the Ag electrode is very slightly improved upon incorporation of MPA into the bronze
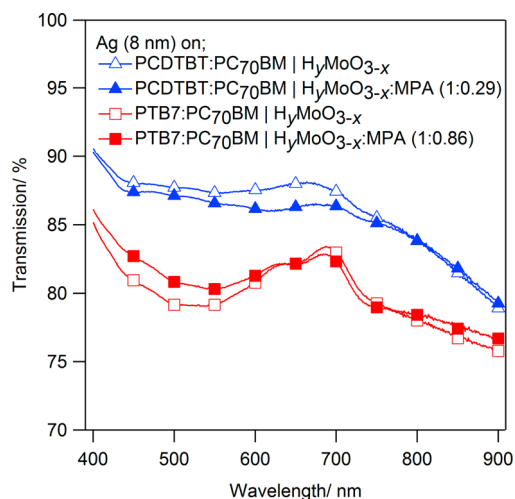

Figure 6. Far-field transparency of 8 nm Ag films deposited on glass| BHJ|H$_y$MoO$_{3-x}$ with and without MPA doping (Mo:MPA ratios of 1:0.29 and 1:0.86 on PCDTBT:PC$_{70}$BM and PTB7:PC$_{70}$BM BHJs, respectively). Absorption by the underlying BHJ|HM$_y$MoO$_{3-x}$ has been subtracted.

underlayer from 79.9% ($\pm$0.4) to 80.5% ($\pm$0.9). Conversely the transparency when deposited onto a PCDTBT:PC$_{70}$BM BHJ is slightly decreased with optimal MPA loading from 85.8% ($\pm$0.5) to 85.6% ($\pm$0.6). The large difference in transparency between electrodes deposited on *different* BHJs can be understood in terms of the large difference in the surface roughness of these BHJ films; 1.5 nm for PCDTBT:PC$_{70}$BM and 2.7 nm for PTB7:PC$_{70}$BM, since even for conformal Ag films the increase in roughness of the underlying substrate will result in increased absorption due to excitation of surface plasmons. For Ag films deposited onto the *same* BHJ the differences in surface roughness are too small to significantly change the transparency because the absolute roughness is 2 orders of magnitude smaller than the wavelength of the incident light. However, these differences are large enough to significantly affect the R_{sheet} since they are of the same order as the metal thickness. Overall the mean transparency and sheet resistance of the electrodes supported on MPA doped H$_y$MoO$_{3-x}$ is superior to that previously reported using an Au seed layer, even without the use of an antireflecting layer, and compare well to that of 8.5 Ω sq^{-1} indium tin oxide coated glass across the wavelength range.[11] These properties, combined with greatly improved stability toward nitrogen and air exposure makes these electrodes an excellent match to the needs of high performance top-illuminated OPVs.

Finally, the performance of these electrodes was evaluated in model top-illuminated OPV devices, with the structure: Al|Cu| Al|BHJ|H$_y$MoO$_{3-x}$|Ag (8 nm), where the BHJ is PTB7:PC$_{70}$BM or PCDTBT:PC$_{70}$BM. AlCuAl was chosen as the back reflective electrode, since it has recently been shown to be a stable low workfunction reflective substrate electrode for top-illuminated OPVs.[37] For both device types the open circuit voltage (V_{oc}) achieved with MPA incorporated into the H$_y$MoO$_{3-x}$ layer is consistent with the highest reported in the literature. For devices based on a PTB7:PC$_{70}$BM BHJ there is a marked improvement in the short-circuit current density (J_{sc}) upon addition of MPA into the H$_y$MoO$_{3-x}$ layer, from 8.27 ($\pm$0.71) to 10.92 mA cm^{-2} ($\pm$0.28), which translates to a commensurate increase in power conversion efficiency (PCE) (Figure 7a). This effect is found to increase with higher
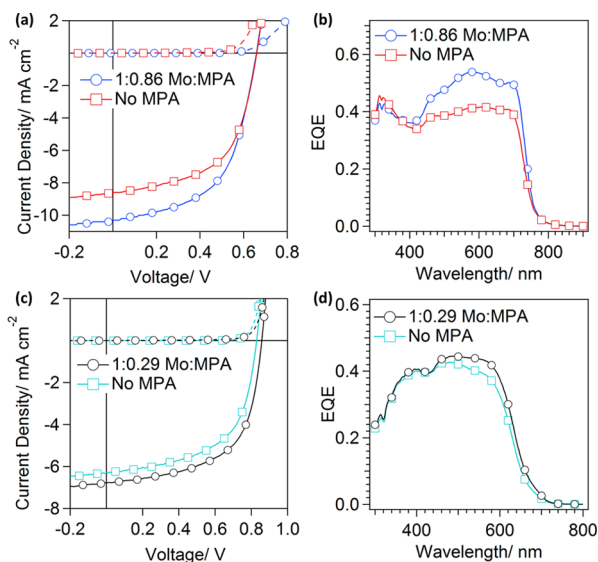
Figure 7. Representative current−voltage and corresponding external quantum efficiency (EQE) data for top-illuminated OPVs with the structure: AlCuAl|PTB7:$PC_{70}BM$|H_yMoO_{3-x}|Ag (8 nm) (a and b) and AlCuAl|PCDTBT:$PC_{70}BM$|H_yMoO_{3-x}|Ag (8 nm) (c and d), with and without MPA in the H_yMoO_{3-x} layer.

loadings of MPA (from 0.15 to 0.86 molecules per Mo) yielding an optimized ratio of 0.86:1 at which point the improvement saturates (Figure S10a). This improvement cannot be attributed to the increased conductivity of the H_yMoO_{3-x} with MPA doping since the contribution to device series resistance from a ∼10 nm H_yMoO_{3-x} layer is calculated to be 0.030 and 0.024 Ω cm^2 for undoped and doped H_yMoO_{3-x} layers respectively, which is small compared to the total series resistance in the OPV (Table 1). This does however explain why the there is no significant improvement in device fill factor (FF) upon MPA doping.[38] It is evident from the external quantum efficiency (EQE) data shown in Figure 7b that the improvement in PCE is due to an increased photoconversion in the longer wavelength region of the spectrum. Similarly, for OPV devices based on a PCDTBT:$PC_{70}BM$ BHJ there is an also an improvement in J_{sc} (Figure 7c) upon incorporation of MPA into the H_yMoO_{3-x} layer, which is optimized for a lower MPA loading, 0.29:1 MPA:Mo (Figure S10b). It is evident from Figure 7d that this improvement is also due to increased photoconversion in the longer wavelength region of the spectrum. Scanning electron microscopy and AFM imaging (Figure S11) of the Ag electrode surface reveals a large difference in surface roughness for Ag films supported on H_yMoO_{3-x} films with and without MPA: 2.8

nm (with MPA) versus 10.1 nm (without). This difference must in large part result from a difference in wetting of the BHJs on the AlCuAl electrode as compared to glass, and is further compelling evidence that adding MPA to H_yMoO_{3-x} greatly improves the film forming properties. The differences in J_{sc} are therefore tentatively ascribed to losses due to plasmon-excitation on the rougher Ag film when the H_yMoO_{3-x} layer is used without MPA. Preliminary stability tests under 1 sun illumination of the PCDTBT:$PC_{70}BM$ OPVs (Figure S12) also show greatly enhanced stability for devices using an MPA doped H_yMoO_{3-x} layer, which is further evidence for improved adhesion at the Ag electrode/H_yMoO_{3-x} interface.

■ CONCLUSIONS

In summary, we have developed a new solution processed layer for top-illuminated organic photovoltaics that combines the function of wide band gap hole-extraction layer with the role of seed layer for the formation of robust 8 nm Ag window electrodes. The advantages of this hybrid electronic material are (i) that it does not add to the complexity of device fabrication, since oxide charge extractions layers are an essential component of high performance OPVs, (ii) it does not use costly materials, such as Au, (iii) and it is compatible with a large range of organic semiconductors, since it is processed from ethanol. We have shown that the key organic component, 3-mercaptopropionic acid, (i) binds to the oxide matrix and silver electrode, promoting silver film formation and robustness at low silver thickness, (ii) reduces the contact resistance at the Ag/molybdenumn oxide bronze interface without significantly adversely affecting the optical properties, and (iii) improves the film forming properties on the surface or organic semiconductor films. Ag film electrodes with a thickness of 8 nm deposited onto this hybrid interlayer have a sheet resistance as low as 9.7 Ohms per square and mean transparency ∼80% over the wavelength range λ = 400−900 nm, *even without the aid of an antireflecting layer*. This performance is superior to that previously reported using a Au seed layer and compares well to that of 8.5 Ω sq^{-1} indium tin oxide coated glass across the wavelength range λ = 400−900 nm. These properties, combined with greatly improved stability toward nitrogen and air exposure makes these electrodes an excellent match to the needs of high performance top-illuminated OPVs. Since solution processed PPVs also employ organic semiconductor charge extraction layers the results are expected to be equally applicable to the advancement of PPVs.

■ EXPERIMENTAL SECTION

Glass substrates were thoroughly cleaned using a four stage process with ultrasonic agitation in (i) deionized water/surfactant (Decon,

Table 1. Key Device Parameters of AlCuAl|PTB7:$PC_{70}BM$|H_yMoO_{3-x}|Ag (8 nm) and AlCuAl|PCDTBT:$PC_{70}BM$|H_yMoO_{3-x}|Ag (8 nm) OPVs[a]

	OPV performance parameters under 1 sun simulated illumination				
BHJ	J_{sc} (mA cm^{-2})	V_{OC} (V)	FF	PCE (%)	R_{series} (Ω cm^2)
			PTB7:$PC_{70}BM$		
no MPA	8.27 (±0.71)	0.64 (±0.02)	0.51 (±0.04)	2.69 (±0.40)	13.46 (±1.32)
with MPA	10.92 (±0.28)	0.65 (±0.03)	0.51 (±0.07)	3.65 (±0.62)	13.24 (±1.82)
			PCDTBT:$PC_{70}BM$		
no MPA	6.06 (±0.28)	0.81 (±0.03)	0.58 (±0.15)	2.88 (±0.15)	13.19 (±0.74)
with MPA	6.56 (±0.40)	0.86 (±0.01)	0.59 (±0.02)	3.33 (±0.17)	11.72 (±0.83)

[a]Series resistance estimated from the gradient of the JV curve under open circuit.

Neutracon) solution, (ii) deionized water, (iii) isopropanol, (iv) and finally acetone vapor, followed by blow drying with nitrogen. Substrates were then UV/O_3 treated to remove surface organic contaminants.

All fabrication and testing was carried out in a N_2 filled glovebox with a base O_2 level of <1 ppm unless otherwise stated. Evaporation of metals was carried out using a CreaPhys Organic molecular evaporator colocated in the same glovebox. The thickness of all vacuum deposited layers was measured using a calibrated quartz-crystal microbalance (QCM) mounted adjacent to the substrates. All metals were thermally evaporated using tungsten boats at a system pressure of $<1 \times 10^{-5}$ mbar.

H_yMoO_{3-x} Synthesis. H_yMoO_{3-x} was synthesized by dispersing molybdenum powder (0.1 g) in ethanol (10 mL) by ultrasonication for 10 min. This solution was heated to 40 °C followed by addition of H_2O_2 (30%, 0.35 mL) under vigorous stirring. The solution turned yellow after 10 h then blue after 48 h. After 72 h reaction the solution was removed from the heat, filtered through 0.2 μm PTFE filter and dried using a rotary evaporator. Solutions with a concentration of 20 mg mL^{-1} in ethanol were prepared by ultrasonic agitation to fully dissolve the powder followed by centrifuging at 10000 rpm for 10 min to remove large particulates.

Thick Film Fabrication. For XPS/UPS and Kelvin probe measurements a 5 mg mL^{-1} solution of H_yMoO_{3-x}, doped with either 0, 10, or 30 mM MPA, was spin coated onto Au (50 nm) electrodes at 800 rpm for 60 s followed by annealing at 80 °C for 10 min under N_2. This was repeated 6 times to achieve thick films. To measure conductivity unipolar diodes were fabricated on Au (50 nm) electrodes by spin-casting H_yMoO_{3-x} (20 mg mL^{-1}) solution with 0, 40, or 120 mM MPA, which correlate to 0:1, 0.29:1, and 0.86:1 MPA:Mo ratios respectively, at 1000 rpm for 60 s, followed by annealing at 80 °C for 10 min under N_2. Onto these was then evaporated Ag (50 nm, 0.1 nm s^{-1})

Thin Film Fabrication. Poly[[4,8-bis[(2-ethylhexyl)oxy]benzo-[1,2-b:4,5-b']dithiophene-2,6-diyl][3-fluoro-2-[(2-ethylhexyl)-carbonyl]thieno[3,4-b]thiophenediyl]]:[6,6]-phenyl-C$_{71}$-butyric acid methyl ester (PTB7:PC$_{70}$BM) and poly[N-9'-heptadecanyl-2,7-carbazole-alt-5,5-(4',7'-di-2-thienyl-2',1',3'-benzothiadiazole)]:[6,6]-phenyl-C$_{71}$-butyric acid methyl ester (PCDTBT:PC$_{70}$BM). For %T and R_{sheet} measurements a BHJ of PTB7:PC$_{70}$BM (4 mg: 6 mg in 0.4 mL dichlorobenzene:diiodooctane, 97:3 vol %, stirred at 60 °C for 16 h prior to use) was deposited on cleaned 18 × 18 mm^2 glass slides by spin coating at 1000 rpm for 60 s followed by 6000 rpm for 4 s then dried under N_2 for 30 min. H_yMoO_{3-x} solution (5 mg mL^{-1}) was then spin coated at 3000 rpm for 60 s followed by annealing at 80 °C for 10 min under N_2 to achieve 10 nm thick films. Ag (8 nm, 0.2 nm s^{-1}) was then deposited. This was repeated with a BHJ of PCDTBT:PC$_{70}$BM (2 mg: 6 mg in 0.5 mL chloroform stirred at 70 °C for 1 h) which was spin-cast dynamically onto a slide spinning at 6000 rpm for 60 s.

OPV Fabrication. Devices were fabricated as above except with an initial electrode deposition by thermally evaporating Al (60 nm, 0.5 nm s^{-1})|Cu (8 nm, 0.1 nm s^{-1})|Al (0.8 nm, 0.02 nm s^{-1}) electrodes without breaking the vacuum between Al and Cu layer deposition. JV curves were measured using a Keithley 2400 source-meter under AM1.5G solar illumination at 100 mW cm^{-2} (1 sun).

EQE measurements were carried out using a Sciencetech SF150 xenon arc lamp and a PTI monochromator, with the monochromatic light intensity calibrated using a Si photodiode (Newport 818-UV). The incoming monochromatic light was chopped at 500 Hz. For signal measurement a Stanford Research Systems SR 830 lock-in amplifier was used.

Tapping mode atomic force microscopy (AFM) imaging was performed in air using an Asylum Research MFP3D. Unless otherwise stated, all surface roughness values are root-mean-square roughness.

Work function measurements were performed using a Kelvin probe referenced to freshly cleaved highly oriented pyrolytic graphite in a nitrogen-filled glovebox colocated with the thermal evaporator.

The X-ray photoelectron spectroscopy (XPS) measurements were performed using a Kratos Axis Ultra DLD spectrometer. The samples were illuminated using X-rays from a monochromated Al Kα source ($h\nu$ = 1486.6 eV) and detected at a takeoff angle of 90 deg. The resolution, binding energy referencing and transmission function of the analyzer were determined using a clean polycrystalline Ag foil. Analysis of the data was undertaken with the CasaXPS package, incorporating Voigt (mixed Gaussian−Lorentzian) lineshapes and a Shirley background. UPS spectra were recorded using UV photons with energy 21.21 eV from a He I plasma source.

■ ASSOCIATED CONTENT

ⓢ Supporting Information

The Supporting Information is available free of charge on the ACS Publications website at DOI: 10.1021/acsami.6b02647.

Grazing incidence X-ray diffraction, XPS, absorption, Tauc plots, AFM, and SEM of H_yMoO_{3-x} films, current−electric field plot of unipolar diodes for conductivity of H_yMoO_{3-x} films, and JV plots of varied loadings of MPA in H_yMoO_{3-x} films (PDF)

■ AUTHOR INFORMATION

Corresponding Author
*E-mail: Ross.Hatton@warwick.ac.uk.

Notes
The authors declare no competing financial interest.

■ ACKNOWLEDGMENTS

■ REFERENCES

(1) Chen, Z. A Mechanical Assessment of Flexible Optoelectronic Devices. *Thin Solid Films* **2001**, *394* (1−2), 201−205.

(2) Lin, H.-W.; Chiu, S.-W.; Lin, L.-Y.; Hung, Z.-Y.; Chen, Y.-H.; Lin, F.; Wong, K.-T. Device Engineering for Highly Efficient Top-Illuminated Organic Solar Cells with Microcavity Structures. *Adv. Mater.* **2012**, *24* (17), 2269−2272.

(3) Barr, M. C.; Howden, R. M.; Lunt, R. R.; Bulovic, V.; Gleason, K. K. Top-Illuminated Organic Photovoltaics on a Variety of Opaque Substrates with Vapor-Printed poly(3,4-Ethylenedioxythiophene) Top Electrodes and MoO$_3$ Buffer Layer. *Adv. Energy Mater.* **2012**, *2* (11), 1404−1409.

(4) Petter Jelle, B. P.; Breivik, C.; Drolsum Røkenes, H. Building Integrated Photovoltaic Products: A State-of-the-Art Review and Future Research Opportunities. *Sol. Energy Mater. Sol. Cells* **2012**, *100* (7465), 69−96.

(5) Nekarda, J.; Reinwand, D.; Grohe, A.; Hartmann, P.; Preu, R.; Trassl, R.; Wieder, S. Industrial PVD Metallization for High Efficiency Crystalline Silicon Solar Cells. *Conf. Rec. IEEE Photovoltaic. Spec. Conf.* **2009**, 000892−000896.

(6) Schubert, S.; Meiss, J.; Müller-Meskamp, L.; Leo, K. Improvement of Transparent Metal Top Electrodes for Organic Solar Cells by Introducing a High Surface Energy Seed Layer. *Adv. Energy Mater.* **2013**, *3* (4), 438−443.

(7) Gupta, K. M.; Gupta, N. *Advanced Electrical and Electronics Materials*; John Wiley & Sons, Inc.: Hoboken, NJ, USA, 2015; pp 1−32.

(8) Lynch, D. W.; Hunter, W. R. Comments on the Optical Constants of Metals and an Introduction to the Data for Several

Metals. In *Handbook of Optical Constants of Solids*; Elsevier, 1985; Vol. 1, pp 275−367.

(9) Jung, K.; Song, H.-J.; Lee, G.; Ko, Y.; Ahn, K.; Choi, H.; Kim, J. Y.; Ha, K.; Song, J.; Lee, J.-K.; Lee, C.; Choi, M. Plasmonic Organic Solar Cells Employing Nanobump Assembly via Aerosol-Derived Nanoparticles. *ACS Nano* **2014**, *8* (3), 2590−2601.

(10) Liu, Y.; Guo, C.-F.; Huang, S.; Sun, T.; Wang, Y.; Ren, Z. A New Method for Fabricating Ultrathin Metal Films as Scratch-Resistant Flexible Transparent Electrodes. *J. Materiomics* **2015**, *1* (1), 52−59.

(11) Kang, J.-W.; Lee, S.-P.; Kim, D.-G.; Lee, S.; Lee, G.-H.; Kim, J.-K.; Park, S.-Y.; Kim, J. H.; Kim, H.-K.; Jeong, Y.-S. Reduction of Series Resistance in Organic Photovoltaic Using Low Sheet Resistance of ITO Electrode. *Electrochem. Solid-State Lett.* **2009**, *12* (3), 64−66.

(12) Xue, J.; Uchida, S.; Rand, B. P.; Forrest, S. R. 4.2% Efficient Organic Photovoltaic Cells With Low Series Resistances. *Appl. Phys. Lett.* **2004**, *84* (16), 3013−3015.

(13) Yang, Y.; Chen, Q.; Hsieh, Y.-T.; Song, T.-B.; De Marco, N.; Zhou, H.; Yang, Y. Multilayer Transparent Top Electrode for Solution Processed perovskite/Cu(In,Ga) (Se,S)2 Four Termianl Tandem Solar Cells. *ACS Nano* **2015**, *9*, 7714.

(14) U.S. Geological Survey. *Mineral Commodity Summaries*; USGS, 2014.

(15) Schubert, S.; Müller-Meskamp, L.; Leo, K. Unusually High Optical Transmission in Ca:Ag Blend Films: High-Performance Top Electrodes for Efficient Organic Solar Cells. *Adv. Funct. Mater.* **2014**, *24* (42), 1−9.

(16) Espinosa, N.; Lenzmann, F. O.; Ryley, S.; Angmo, D.; Hösel, M.; Søndergaard, R. R.; Huss, D.; Dafinger, S.; Gritsch, S.; Kroon, J. M.; Jørgensen, M.; Krebs, F. C. OPV for Mobile Applications: An Evaluation of Roll-to-Roll Processed Indium and Silver Free Polymer Solar Cells through Analysis of Life Cycle, Cost and Layer Quality Using Inline Optical and Functional Inspection Tools. *J. Mater. Chem. A* **2013**, *1* (24), 7037−7049.

(17) Youn, H.; Park, H. J.; Guo, L. J. Organic Photovoltaic Cells: From Performance Improvement to Manufacturing Processes. *Small* **2015**, *11* (19), 2228−2246.

(18) Xie, F.; Choy, W. C. H.; Wang, C.; Li, X.; Zhang, S.; Hou, J. Low-Temperature Solution-Processed Hydrogen Molybdenum and Vanadium Bronzes for an Efficient Hole-Transport Layer in Organic Electronics. *Adv. Mater.* **2013**, *25* (14), 2051−2055.

(19) Vasilopoulou, M.; Soultati, A.; Georgiadou, D. G.; Stergiopoulos, T.; Palilis, L. C.; Kennou, S.; Stathopoulos, N. a.; Davazoglou, D.; Argitis, P. Hydrogenated under-Stoichiometric Tungsten Oxide Anode Interlayers for Efficient and Stable Organic Photovoltaics. *J. Mater. Chem. A* **2014**, *2* (6), 1738−1749.

(20) Steim, R.; Kogler, F. R.; Brabec, C. J. Interface Materials for Organic Solar Cells. *J. Mater. Chem.* **2010**, *20* (13), 2499−2512.

(21) Zilberberg, K.; Meyer, J.; Riedl, T. Solution Processed Metal-Oxides for Organic Electronic Devices. *J. Mater. Chem. C* **2013**, *1* (32), 4796−4815.

(22) Wang, J.; Zhang, J.; Meng, B.; Zhang, B.; Xie, Z.; Wang, L. Facile Preparation of Molybdenum Bronzes as an Efficient Hole Extraction Layer in Organic Photovoltaics. *ACS Appl. Mater. Interfaces* **2015**, *7* (24), 13590−13596.

(23) Soultati, A.; Douvas, A. M.; Georgiadou, D. G.; Palilis, L. C.; Bein, T.; Feckl, J. M.; Gardelis, S.; Fakis, M.; Kennou, S.; Falaras, P.; Stergiopoulos, T.; Stathopoulos, N. a.; Davazoglou, D.; Argitis, P.; Vasilopoulou, M. Solution-Processed Hydrogen Molybdenum Bronzes as Highly Conductive Anode Interlayers in Efficient Organic Photovoltaics. *Adv. Energy Mater.* **2014**, *4* (3), 1300896.

(24) Vasilopoulou, M.; Douvas, A. M.; Georgiadou, D. G.; Palilis, L. C.; Kennou, S.; Sygellou, L.; Soultati, A.; Kostis, I.; Papadimitropoulos, G.; Davazoglou, D.; Argitis, P. The Influence of Hydrogenation and Oxygen Vacancies on Molybdenum Oxides Work Function and Gap States for Application in Organic Optoelectronics. *J. Am. Chem. Soc.* **2012**, *134* (39), 16178−16187.

(25) Li, X.; Xie, F.; Zhang, S.; Hou, J.; Choy, W. C. MoO_x and V_2O_x as Hole and Electron Transport Layers through Functionalized Intercalation in Normal and Inverted Organic Optoelectronic Devices. *Light: Sci. Appl.* **2015**, *4* (4), e273.

(26) Li, X.; Xie, F.; Zhang, S.; Hou, J.; Choy, W. C. H. Over 1.1 eV Workfunction Tuning of Cesium Intercalated Metal Oxides for Functioning as Both Electron and Hole Transport Layers in Organic Optoelectronic Devices. *Adv. Funct. Mater.* **2014**, *24* (46), 7348−7356.

(27) Fleisch, T. H. An XPS Study of the UV Reduction and Photochromism of MoO3 and WO3. *J. Chem. Phys.* **1982**, *76* (2), 780−786.

(28) Bournel, F.; Laffon, C.; Parent, P.; Tourillon, G. Adsorption of Some Substituted Ethylene Molecules on Pt(111) at 95 K Part 1: NEXAFS, XPS and UPS Studies. *Surf. Sci.* **1996**, *350* (1−3), 60−78.

(29) Kanninen, L.; Jokinen, N.; Ali-Löytty, H.; Jussila, P.; Lahtonen, K.; Hirsimäki, M.; Valden, M.; Kuzmin, M.; Pärna, R.; Nõmmiste, E. Adsorption Structure and Bonding of Trimesic Acid on Cu(100). *Surf. Sci.* **2011**, *605* (23−24), 1968−1978.

(30) Greiner, M. T.; Chai, L.; Helander, M. G.; Tang, W. M.; Lu, Z. H. Metal/metal-Oxide Interfaces: How Metal Contacts Affect the Work Function and Band Structure of MoO3. *Adv. Funct. Mater.* **2013**, *23* (2), 215−226.

(31) Kim, J. S.; Lägel, B.; Moons, E.; Johansson, N.; Baikie, I. D.; Salaneck, W. R.; Friend, R. H.; Cacialli, F. Kelvin Probe and Ultraviolet Photoemission Measurements of Indium Tin Oxide Work Function: A Comparison. *Synth. Met.* **2000**, *111*, 311−314.

(32) Ito, E.; Oji, H.; Hayashi, N.; Ishii, H.; Ouchi, Y.; Seki, K. Electronic Structures of TPD/metal Interfaces Studied by Photoemission and Kelvin Probe Method. *Appl. Surf. Sci.* **2001**, *175−176*, 407−411.

(33) Braun, S.; Salaneck, W. R.; Fahlman, M. Energy-Level Alignment at Organic/metal and Organic/organic Interfaces. *Adv. Mater.* **2009**, *21* (14−15), 1450−1472.

(34) Scharber, M. C.; Mühlbacher, D.; Koppe, M.; Denk, P.; Waldauf, C.; Heeger, A. J.; Brabec, C. J. Design Rules for Donors in Bulk-Heterojunction Solar Cells - Towards 10% Energy-Conversion Efficiency. *Adv. Mater.* **2006**, *18* (6), 789−794.

(35) Kasl, C.; Hoch, M. J. R. Effects of Sample Thickness on the van Der Pauw Technique for Resistivity Measurements. *Rev. Sci. Instrum.* **2005**, *76* (3), 1−5.

(36) Gonella, G.; Cavalleri, O.; Terreni, S.; Cvetko, D.; Floreano, L.; Morgante, a.; Canepa, M.; Rolandi, R. High Resolution X-Ray Photoelectron Spectroscopy of 3-Mercaptopropionic Acid Self-Assembled Films. *Surf. Sci.* **2004**, *566−568*, 638−643.

(37) Tyler, M. S.; Hutter, O. S.; Walker, D. M.; Hatton, D. R. a. A Silver-Free, Reflective Substrate Electrode for Electron Extraction in Top-Illuminated Organic Photovoltaics. *ChemPhysChem* **2015**, *16* (6), 1203−1209.

(38) Wojciechowski, K.; Saliba, M.; Leijtens, T.; Abate, A.; Snaith, H. J. Sub-150 °C Processed Meso-Superstructured Perovskite Solar Cells with Enhanced Efficiency. *Energy Environ. Sci.* **2014**, *7* (3), 1142−1147.